AsH_3 Ultraviolet Photochemistry†

L. A. Smith-Freeman, W. P. Schroeder, and C. Wittig*

Department of Chemistry, University of Southern California, Los Angeles, California 90089

Received: October 26, 2008; Revised Manuscript Received: December 22, 2008

High-*n* Rydberg time-of-flight spectroscopy has been used to study the 193.3 nm photolysis of AsH_3. The center-of-mass translational energy distribution for the 1-photon process, $AsH_3 + h\nu \rightarrow AsH_2 + H$, $P(E_{c.m.})$, indicates that AsH_2 internal excitation accounts for ~64% of the available energy [i.e., $h\nu - D_0(H_2As - H)$]. Secondary AsH_2 photodissociation also takes place. Analyses of superimposed structure atop the broad $P(E_{c.m.})$ distribution suggest that AsH_2 is formed with significant *a*-axis rotation as well as bending excitation. Comparison of the results obtained with AsH_3 versus those of the lighter group-V hydrides (NH_3, PH_3) lends support to the proposed mechanisms. Of the group-V hydrides, AsH_3 lies intermediate between the nonrelativistic and relativistic regimes, requiring high-level electronic structure theory.

I. Introduction

The ultraviolet photolysis of gaseous AsH_3 is germane to the fabrication of semiconductor and electro-optical devices.[1−4] For example, it has been demonstrated that the 193.3 nm irradiation of AsH_3 can be used to stimulate and manipulate the growth of III−V semiconductor compounds, such as GaAs, InGaAs, and InGaAsP, etc., during metalorganic chemical vapor deposition.[2,3] AsH_3 is of fundamental scientific interest, as well. For example, a sensible goal is a quantitative understanding of how molecular properties and photochemical and photophysical mechanisms vary when the lightest group-V hydride, NH_3, is replaced by progressively heavier counterparts (PH_3, AsH_3, SbH_3, BiH_3), i.e., those that span the nonrelativistic and relativistic regimes. High-quality experimental data for the full complement of group-V hydrides would comprise a benchmark against which theoretical models could be tested.

Although there has been a great deal of theoretical and experimental research on NH_3, much less has been done with the heavier group-V hydrides. Experimentalists must contend with toxicity and sample preparation/handling issues, and theoreticians must contend with large numbers of electrons and relativistic effects. The increase in nuclear charge has a pronounced effect on electron velocities, especially for *s*-orbitals. As speed increases (approaching the speed of light for the heaviest elements), radii decrease and orbital energies are lowered.[5,6] This orbital contraction shields the nuclear charge from the valence electrons, leading to ionization energies, bond energies, and orbital energies that do not follow trends that have been established for lighter atoms.[5,6]

Extensive research on the photochemistry and photophysics of NH_3 has yielded high-quality potential energy surfaces (PESs) and a consensus regarding the properties of the lowest excited surfaces and the dynamical processes that transpire on them.[7−14] This system is a textbook example of predissociation and nonadiabatic dynamics. The ground-state electron configuration is $(1a_1)^2(2a_1)^2(1e)^4(3a_1)^2$ (C_{3v} notation). The promotion of an electron from the lone pair orbital $3a_1$ ($1a_2$ in the D_{3h} limit) to the 3s a_1' Rydberg orbital accounts for the $\tilde{A}\,^1A_2'' \leftarrow \tilde{X}\,^1A_1$ transition, with its pyramidal-to-planar geometry change. Consequently, the $\tilde{A} \leftarrow \tilde{X}$ absorption spectrum displays a prominent progression in the ν_2 umbrella mode.

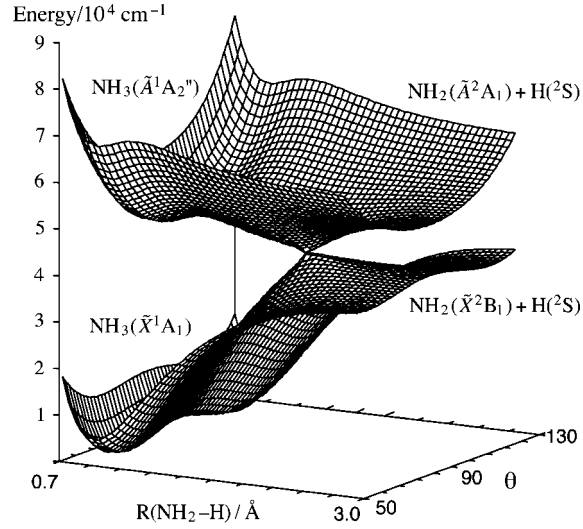

Figure 1. Conical intersection between the ground and excited surfaces of NH_3 is indicated (adapted from reference 16). Vertical excitation from the NH_3 $\tilde{X}\,^1A_1$ ground vibrational level to $\tilde{A}\,^1A_2''$ can lead to dissociation to $NH_2(\tilde{A}\,^2A_1)$ via adiabatic paths, or to $NH_2(\tilde{X}\,^2B_1)$ via nonadiabatic paths that pass near the conical intersection. θ is the angle between a NH bond and the normal to the trigonal plane. $\theta = 90°$ corresponds to planar geometry.

Vibrational levels of the $\tilde{A}\,^1A_2''$ state are predissociated to the extent that there is no discernible rotational structure.[11] There is a small barrier to dissociation on this surface that arises from the Rydberg-to-valence transformation that accompanies lengthening of the N−H bond.[7,9,15] The height of this barrier increases with an out-of-plane bend angle (minimizing at planar geometries). For the $\tilde{A}\,^1A_2''$ vibrational levels $\upsilon_2' = 1$ and 2 and dissociation proceeds via tunneling through the barrier. An $\tilde{A}/\tilde{X}$ conical intersection also plays a significant role.[7−10]

Referring to Figure 1, in C_{2v} symmetry, $NH_3(\tilde{A})$ correlates diabatically with $NH_2(\tilde{X}\,^2B_1)$, whereas $NH_3(\tilde{X})$ correlates diabatically with $NH_2(\tilde{A}\,^2A_1)$. For nonplanar geometries ($\theta \neq 90°$ in Figure 1), the NH_3 $\tilde{X}$ and $\tilde{A}$ states are each of the same symmetry, and there is an avoided crossing. Consequently, $NH_3(\tilde{A})$ correlates adiabatically with $NH_2(\tilde{A})$, whereas $NH_3(\tilde{X})$

† Part of the "Max Wolfsberg Festschrift".

* Corresponding author. E-mail: wittig@usc.edu

10.1021/jp8094769 CCC: $40.75
Published on Web 02/04/2009

TABLE 1: Equilibrium H−M−H Angles for M = N, P, and As and Related Electronic States[a]

$NH_3(\tilde{X}^1A_1)$	107°	
$NH_3(\tilde{A}^1A_2'')$	120°	$NH_3(\tilde{A}) \rightarrow NH_2(\tilde{X})$
$NH_2(\tilde{X}^2B_1)$	103.4°	θ_{H-N-H}^{equil}: 120° → 103.4°
$NH_2(\tilde{A}^2A_1)$	144°	
$PH_3(\tilde{X}^1A_1)$	93.5°	
$PH_3(\tilde{A}^1A_1)$	114°	$PH_3(\tilde{A}) \rightarrow PH_2(\tilde{X})$
$PH_2(\tilde{X}^2B_1)$	91.4°	θ_{H-P-H}^{equil}: 114° → 91.4°
$PH_2(\tilde{A}^2A_1)$	123.1°	
$AsH_3(\tilde{X}^1A_1)$	92.1°	
$AsH_3(\tilde{A}^1E)$	112°	$AsH_3(\tilde{A}) \rightarrow AsH_2(\tilde{X})$
$AsH_2(\tilde{X}^2B_1)$	90.4°	θ_{H-As-H}^{equil}: 112° → 90.4°
$AsH_2(\tilde{A}^2A_1)$	123°	

[a] See text for details and references.

correlates adiabatically with $NH_2(\tilde{X})$. Figure 1 illustrates these aspects of the surfaces.[16]

The barrier and conical intersection influence the dissociation dynamics of $NH_3(\tilde{A})$. Biesner et al. studied this for $0 \leq v_2' \leq 6$ using H atom photofragment translational energy spectroscopy.[17] They found that NH_2 is born with significant internal excitation, mainly in the form of *a*-axis rotation. They concluded that NH_3 out-of-plane bending is encouraged by the shape of the potential in the vicinity of the conical intersection, resulting in considerable $NH_2(\tilde{X})$ *a*-axis rotation. In contrast, near-planar dissociation leads to NH_2 with modest *a*-axis rotation. It is intuitive that umbrella mode vibrational excitation correlates with *a*-axis rotation. It should be noted that competition between adiabatic and nonadiabatic pathways is energy-dependent, with $NH_2(\tilde{A})$ accounting for 10−30% of the NH_2 product when NH_3 is excited to $v_2' = 6$ of its $\tilde{A}$ state.[17] These experimental findings are in accord with theoretical calculations and results from other experiments.[7,12,14,17]

The dissociation dynamics of PH_3 are similar to those of NH_3, albeit with several important differences. The $\tilde{A} \leftarrow \tilde{X}$ transition involves the promotion of the lone pair orbital $5a_1$ to the 4s a_1 Rydberg orbital, and calculations indicate a small barrier on the $PH_3(\tilde{A})$ surface.[18] The height of this barrier is comparable to the zero-point energy of the stretching vibration. The $\tilde{A} \leftarrow \tilde{X}$ absorption spectrum is a broad continuum, consistent with rapid $\tilde{A}$ dissociation.[19] Whereas the $NH_3(\tilde{A})$ equilibrium geometry is planar, the $PH_3(\tilde{A})$ equilibrium geometry has been calculated to be nonplanar ($\theta_{H-P-H} \sim 114°$).[18] The ground state of PH_3^+ is also nonplanar,[20] so it is intuitive that $PH_3(\tilde{A})$ is nonplanar. The $\tilde{A} \leftarrow \tilde{X}$ transition increases the equilibrium bond angle from 93.5° to 114°,[18] which ensures significant ν_2 vibrational excitation. Table 1 gives values of relevant equilibrium angles for NH_3, PH_3, and AsH_3.

It has been suggested that the PH_3 $\tilde{A}/\tilde{X}$ conical intersection affects the dissociation dynamics in a manner that is analogous to the case of NH_3. Several experimental studies have shown that PH_2 is born with substantial internal excitation,[21−23] although the exact nature of this excitation is more difficult to discern than for NH_2. Lambert et al.[21] investigated the UV photolysis of PH_3 by using high-*n* Rydberg time-of-flight (HRTOF) spectroscopy. They found that $PH_2(\tilde{X})$ rovibrational excitation accounts for, on average, ∼62% of the available energy. Structured translational energy distributions indicated significant $PH_2(\tilde{X})$ *a*-axis rotation, as well as bending excitation. It was postulated that $PH_2(\tilde{X})$ vibrational excitation is due to the change in bond angle: from 114° in $PH_3(\tilde{A})$ to 91.4° in $PH_2(\tilde{X})$. The data also showed evidence of $PH_2(\tilde{X})$ photodissociation.

The scarcity of experimental and theoretical data on AsH_3 is striking compared to what is available for the lighter group-V hydrides. For example, no information concerning dissociation pathways on $\tilde{A}$ and $\tilde{X}$ surfaces is available. However, taking cues from PH_3 and NH_3, it is *assumed* that there is a small barrier to dissociation on $\tilde{A}$ and an $\tilde{A}/\tilde{X}$ conical intersection. The $\tilde{A} \leftarrow \tilde{X}$ absorption is continuous, with weak superimposed structure, as with PH_3. Analyses of AsH_3 and PH_3 absorption spectra reveal that $\tilde{\nu}_2' \sim \tilde{\nu}_2''/2$ in these cases, whereas $\tilde{\nu}_2' \sim \tilde{\nu}_2''$ for NH_3.[19] Humphries et al. have proposed that the $\tilde{A}$ states of AsH_3 and PH_3 are pyramidal, with $\tilde{A} \leftarrow \tilde{X}$ transitions terminating on levels that lie above the inversion barrier.[19] In addition, the AsH_3 photoelectron spectrum suggests a pyramidal geometry.[24,25] The equilibrium bond angle for $AsH_3(\tilde{A})$ is *assumed* to be 112° on the basis of the AsH_3^+ bond angle[26] and the geometry of $PH_3(\tilde{A})$. The equilibrium bond angle for the AsH_3 $\tilde{X}$ state is 92.1°.[27] It is noteworthy that a calculation of the lowest excited singlet indicates that it has *E* symmetry, which would make this case quite different from the lowest excited singlets of NH_3 and PH_3. This will be discussed later.

Velocity-aligned Doppler spectroscopy has been used by Koplitz et al. to examine the 193.3 nm (hereafter referred to simply as 193 nm) photodissociation of AsH_3.[28] Their results indicate that AsH_2 fragments are formed with average internal energies ∼2/3 the available energy. However, the low resolution of the method precluded a determination of the internal energy distribution. An AsH_2 $\tilde{A} \rightarrow \tilde{X}$ emission spectrum has been recorded by Ni et al. following 193 nm photolysis of AsH_3.[29] Both v_2' and v_2'' progressions were evident, as well as spectral features that were assigned to As. Photolysis of AsH_2 was suggested as a possible mechanism for the As emission.

In the study reported here, the 193 nm photodissociation of AsH_3 has been examined using HRTOF spectroscopy. Figure 2 shows a number of possible products.[24,26,30−35] Note that the photon energy is substantially larger than the AsH_3 bond dissociation energy. The results indicate that AsH_2 is produced with significant internal excitation. $AsH_2(\tilde{A})$ is also produced, but it is a minor channel. The center-of-mass (c.m.) translational energy distribution, $P(E_{c.m.})$, consists of partially resolved structure superimposed on a broad background. Unambiguous assignment is not feasible because the structured features are broad and of modest signal-to-noise ratio (S/N) and there is a significant amount of secondary photolysis.

In consideration of the photodissociation dynamics of NH_3 and PH_3, it is suggested that the main features arise from $AsH_2(\tilde{X})$ with substantial *a*-axis rotation as well as bending excitation. Secondary photolysis of $AsH_2(\tilde{X})$ yields AsH. In light of the similarities between the present results and those obtained with PH_3, it is interesting that the AsH_3 $\tilde{A}$ state has been calculated to be ^1E,[26] whereas the PH_3 $\tilde{A}$ state is $^1A_1$. The AsH_3 system lies intermediate between nonrelativistic and relativistic regimes. An important goal is that this system achieves the same degree of accord between theory and experiment enjoyed by lighter counterparts.

II. Experimental

The HRTOF arrangement shown in Figure 3 has been discussed previously,[36] so only details that are relevant to the present study are given here. A pulsed valve (General Valve, 0.8 mm orifice) expanded mixtures of AsH_3 (Matheson Tri-Gas, 99.999%) dilute in a carrier gas (10% in H_2, 5% in H_2, and 5% in Ar). The molecular beam was collimated 2 cm downstream from the nozzle by a 1-mm-diameter skimmer. At the interaction region, 5 cm downstream from the skimmer, the molecular beam was intersected by the outputs of three pulsed laser systems.

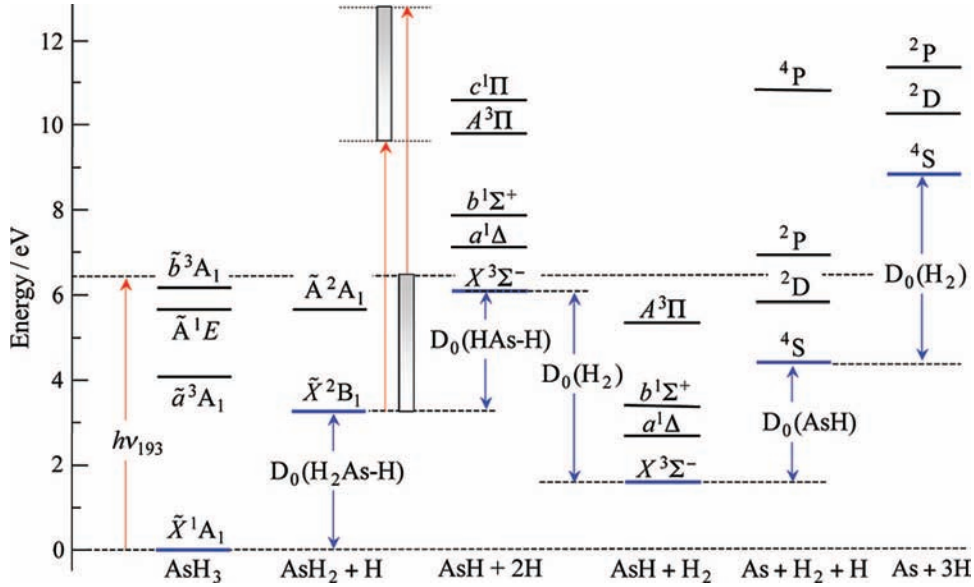

Figure 2. Energies relevant to 193 nm photolysis of AsH_3 are indicated, including product species that can undergo secondary photodissociation. The two red arrows and shaded rectangles to the right of the $AsH_2 + H$ column indicate the range of energies associated with internally excited AsH_2. Energy values were obtained as follows: AsH_3 excited states, ref 26; $D_0(H_2As - H)$, ref 24; $AsH_2(\tilde{A})$, ref 30; $D_0(HAs - H)$, ref 24; $D_0(As - H)$, ref 24; AsH excited states, ref 31−34; As excited states, ref 35.

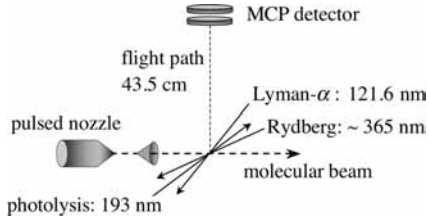

Figure 3. Experimental arrangement.

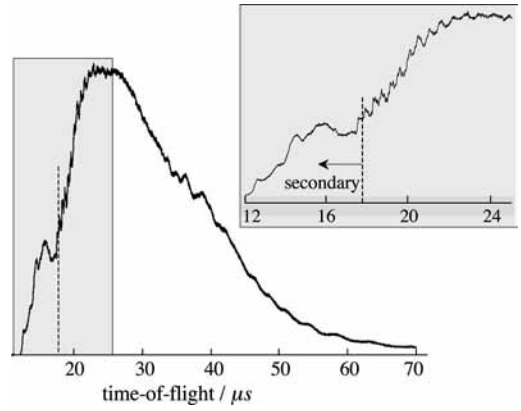

Figure 4. HRTOF spectrum obtained using 5% AsH_3 and 193 nm photolysis: Results from 121 000 laser firings were summed to obtain the trace. The 193 nm energy ranged between 2.2 and 2.5 mJ. The vertical dashed lines indicate the earliest possible arrival time compatible with 1-photon AsH_3 photodissociation.

Photolysis radiation was from an ArF excimer laser (Lambda Physik Compex 201). HRTOF spectroscopy probed nascent H atoms by using sequential excitation to high-n Rydberg levels: 121.6 nm radiation excited H atoms (Lyman-α), and ∼365 nm radiation promoted the excited H atoms to a Rydberg state with $n \sim 50$. Two Nd:YAG pump lasers (Continuum Powerlite 8010 and 9010) and two dye lasers were used for this "tagging" of the H atoms. The output of one dye laser (Continuum ND6000, LDS 750 dye) was frequency-doubled in a KDP-C crystal, producing 364.8 nm radiation. This was focused into a 10 cm tripling cell, where Lyman-α radiation was generated by nonresonant frequency-tripling in Kr. Dissociation of AsH_3 by 121.6 nm radiation was negligible due to the low efficiency of the third harmonic generation. The output of the second dye laser (Continuum ND6000, LDS 750 dye) was frequency-doubled, yielding the Rydberg (∼365 nm) radiation.

Metastable H atoms that traverse the 43.5 cm flight tube (perpendicular to the interaction region; see Figure 3) are field-ionized and detected with near-unit efficiency by two back-to-back microchannel plates in a chevron configuration. A weak dc field applied to a pair of electrodes surrounding the interaction region eliminates ion background signals and makes space anisotropic for high-n Rydberg atoms. This enables high-n Rydberg atoms to be prepared with large orbital angular momentum values and, consequently, long spontaneous emission lifetimes after they leave the interaction region.

III. Results

An HRTOF spectrum for the photolysis of jet-cooled AsH_3 is presented in Figure 4. Vertical dashed lines indicate the earliest arrival time that can be attributed to primary photolysis using $D_0(H_2As - H) = 74.9 \pm 0.2$ kcal/mol.[24] The signal that precedes the dashed line is evidence of secondary photolysis. Many such spectra were recorded, and no qualitative differences were observed. The one shown in Figure 4 is one of the better ones insofar as S/N is concerned.

Figure 5 shows HRTOF spectra for the photolysis of AsH_3 (10% in H_2). These traces were obtained using 193 nm energies of 0.5 and 4.2 mJ. The 193 nm radiation is focused using a 100 cm focal length lens, resulting in fluences of ∼5 and ∼40 J/cm^{-2}, respectively. Reducing the photolysis fluence lessens the production of fast H atoms that derive from secondary photolysis. However, the broad unstructured one-photon signal was not simplified; it was just of lower intensity. Analogous spectra collected using supersonic expansions of 5% AsH_3 in H_2 and 5% AsH_3 in Ar showed no discernible variations from the spectrum in Figure 4, so they are not presented. The spectrum in Figure 4 was converted to the c.m. translational energy distribution shown in Figure 6a by using the formulas

$$E_{c.m.} = \frac{1}{2} m_H \left((d/t)^2 + v_{mb}^2\right)\left(1 + m_H/m_{AsH_2}\right) \quad (1)$$

$$P(E_{c.m.}) \propto t^3 f(t(E_{c.m.})) \quad (2)$$

where v_{mb} is the molecular beam velocity, d is the length of the flight tube, and t is the H-atom arrival time. Referring to eq 2, the measured TOF distribution, $f(t)$, is converted to the corresponding c.m. translational energy distribution, $P(E_{c.m.})$, by using the time-to-energy Jacobian, which is proportional to t^3, and the relationship between t and $E_{c.m.}$ given in eq 1. Note: $P(E_{c.m.})$ applies only to those channels that yield H atoms.

The black dashed line to the right of the red box in Figure 6a indicates the maximum $E_{c.m.}$ allowed by energy conservation when the H atoms result from primary photolysis. Translational energies in excess of this value derive from secondary photolysis. The inset in Figure 6a shows a fairly abrupt termination of $P(E_{c.m.})$ at 51 800 ± 500 cm^{-1}, corresponding to dissociation of AsH_2 with internal energies near D_0(H-AsH) = 66.5 ± 0.02 kcal/mol[24] and negligible AsH internal excitation. The value 51 800 ± 500 cm^{-1} was obtained by deconvoluting the data to account for instrument resolution.

Background subtraction was used to elucidate peaks in the ranges 1000−10 000 cm^{-1} (Figure 6b) and 14 000−24 000 cm^{-1} (Figure 6c). The average spacing between peaks in the high-energy region is ∼1000 cm^{-1}, in rough accord with the AsH_2 bend frequency.[30] In the low-energy region, the spacing is ∼360 cm^{-1} for the range 1500−5000 cm^{-1}. We interpret this as due to *a*-axis rotation in $AsH_2(\tilde{X})$, as discussed in the next section.

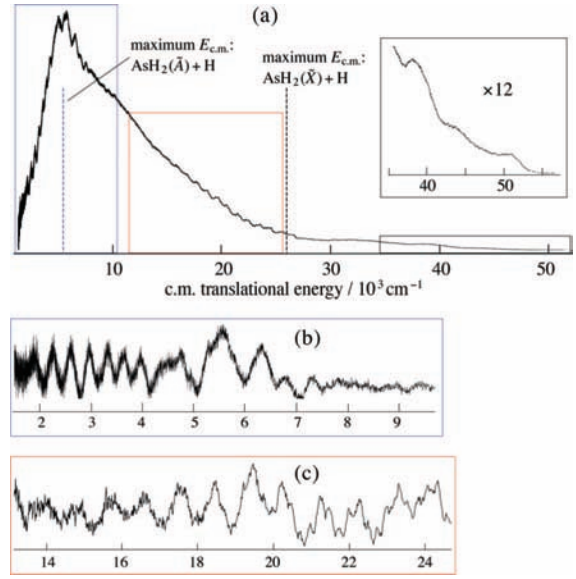

Figure 6. (a) The HRTOF spectrum in Figure 4 has been converted to $P(E_{c.m.})$; inset: expanded view of the high-energy region. The black dashed line to the right of the red box indicates the maximum $E_{c.m.}$ available to a one-photon process. The blue dashed line in the blue box indicates the maximum $E_{c.m.}$ available to the $AsH_2(\tilde{A})$ channel via a one-photon process. (b) This pertains to the blue box in panel a. To highlight peaks, the underlying continuous distribution has been suppressed (see text). (c) This pertains to the red box in panel a. To highlight peaks, the underlying continuous distribution has been suppressed.

IV. Discussion

The unambiguous identification of the participating pathways and mechanisms in the 193 nm photodissociation of AsH_3, as well as its nascent photofragments, is difficult for several reasons. First, the photon energy exceeds greatly the bond dissociation energies of AsH_3 and AsH_2, thereby enabling highly internally excited fragments to be produced, with a multitude of possible reaction channels. Second, theoretical calculations on AsH_3 and AsH_2 are limited. Third, the presence of significant secondary photolysis adds an unappreciated subtlety to the assignment of the c.m. translational energy distribution. The eye is drawn to the peaks, yet the broad background contains nearly all of the signal and, therefore, the real story. The above points compromise our ability to extract product internal energy distributions.

The goal of this section is a qualitative understanding of the photoinitiated decomposition dynamics of the AsH_3 system, in particular vis-à-vis its NH_3 and PH_3 counterparts. The NH_3 system has received a great deal of attention owing to its experimental accessibility and its relatively straightforward electronic structure. At the same time, it is important to examine heavier counterparts, and AsH_3 is a good candidate, because it lies intermediate between nonrelativistic and relativistic regimes.

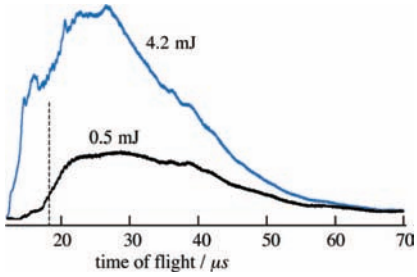

Figure 5. HRTOF spectra for photolysis energies of 0.5 and 4.2 mJ: 135 000 and 116 000 laser firings, respectively.

Primary Photolysis: $AsH_3 \rightarrow AsH_2 + H$. The $P(E_{c.m.})$ distribution shown in Figure 6a is broad, with partially resolved structure and a maximum at low $E_{c.m.}$. Despite the presence of secondary photolysis, an estimate of the "center-of-gravity" of the distribution indicates that AsH_2 internal excitation accounts for ∼64% of the available energy [i.e., $E_{avail} = h\nu - D_0(H_2As - H)$]. This is in agreement with the qualitative result of Koplitz et al.,[28] who reported that internal excitation accounts for ∼2/3 of the available energy.

Following the absorption of a 193 nm (6.42 eV) photon, the following channels are energetically accessible (also see Figure 2):

$$AsH_3(\tilde{X}\,^1A_1) + h\nu_{193} \rightarrow AsH_2(\tilde{X}\,^2B_1) + H \quad (3)$$

$$AsH_3(\tilde{X}\,^1A_1) + h\nu_{193} \rightarrow AsH_2(\tilde{A}\,^2A_1) + H \quad (4)$$

$$AsH_3(\tilde{X}\,^1A_1) + h\nu_{193} \rightarrow AsH(X\,^3\Sigma^-) + H_2 \quad (5)$$

$$AsH_3(\tilde{X}\,^1A_1) + h\nu_{193} \rightarrow AsH(X\,^3\Sigma^-) + H + H \quad (6)$$

$$AsH_3(\tilde{X}\,^1A_1) + h\nu_{193} \rightarrow AsH(a\,^1\Delta) + H_2 \quad (7)$$

$$AsH_3(\tilde{X}\,^1A_1) + h\nu_{193} \rightarrow AsH(b\,^1\Sigma^+) + H_2 \quad (8)$$

$$AsH_3(\tilde{X}\,^1A_1) + h\nu_{193} \rightarrow AsH(A\,^3\Pi) + H_2 \quad (9)$$

$$AsH_3(\tilde{X}\,^1A_1) + h\nu_{193} \rightarrow AsH(c\,^1\Pi) + H_2 \quad (10)$$

$$AsH_3(\tilde{X}\,^1A_1) + h\nu_{193} \rightarrow As(^4S) + H_2 + H \quad (11)$$

$$AsH_3(\tilde{X}\,^1A_1) + h\nu_{193} \rightarrow As(^2D) + H_2 + H \quad (12)$$

Given that $AsH_2(\tilde{A})$ lies 19 909 cm^{-1} above $AsH_2(\tilde{X})$,[30] the maximum $E_{c.m.}$ that is compatible with reaction 4 is 5600 cm^{-1}

(see Figure 2). The distribution shown in Figure 6 indicates that reaction 3 dominates, with high $AsH_2(\tilde{X})$ rovibrational excitation. This is reasonable in light of the photodissociation dynamics of PH_3[21−23] and NH_3.[12−14,17]

Ultraviolet photoexcitation results in a change of equilibrium geometry. The $AsH_3(\tilde{X})$ electron configuration is $\cdots (a_1)^2(e)^4(a_1)^2$, and the equilibrium value of the θ_{H-As-H} angle is 92.1°.[27] According to the Walsh diagram for this system, promotion of an a_1 lone pair electron to the Rydberg a_1 orbital increases the θ_{H-As-H} equilibrium angle.[37] This will excite the ν_2 umbrella mode, as in the analogous $\tilde{A} \leftarrow \tilde{X}$ transitions in NH_3 and PH_3.[9,19] It should be noted that the promotion of an a_1 lone pair electron to other excited orbitals in this energy region might also result in umbrella mode excitation.

The photoinitiated dissociation dynamics of NH_3 provides insight. The NH_3 $\tilde{A} \leftarrow \tilde{X}$ absorption spectrum exhibits a resolved ν_2 progression that reflects the pyramidal-to-planar geometry change. Experimental studies of the state-selected (i.e., υ_2') photodissociation of $NH_3(\tilde{A})$ confirm that NH_2 is formed with significant internal excitation that is primarily in the form of *a*-axis rotation.[12,17] Not surprisingly, the amount of NH_2 internal excitation increases with photon energy. Moreover, excitation of the NH_2 bend has been observed following dissociation via higher υ_2'.[14,16,17] Theory and experiment confirm that dissociation commencing from the $\tilde{A}$ surface is sensitive to (i) its vibrational state; (ii) geometries and motions sampled during fragmentation; (iii) the topography of the conical intersection region; and (iv) competition between adiabatic and nonadiabatic pathways.[7−14,16,17]

Dissociation to ground electronic state products is governed by the $\tilde{A}/\tilde{X}$ conical intersection. For example, trajectory calculations of Biesner et al. illustrate the intersection's influence on energy disposal into product degrees of freedom.[12] Referring to Figure 1, trajectories are funneled toward the intersection, and nonadiabatic transitions are facilitated by near-planar geometry. Dissociation to $NH_2(\tilde{X})$ can occur either on the first pass through the intersection region or, if this fails, on a subsequent pass. The intersection region has a large gradient in the angular coordinate, and this promotes $NH_2(\tilde{X})$ *a*-axis rotation. Trajectories that fail to emerge on the $NH_2(\tilde{A})$ asymptote in the first pass through the conical intersection region can sample more of the $\tilde{A}$ surface.[12]

Dissociation of NH_3 from higher υ_2' leads to NH_2 with larger amounts of vibrational and electronic excitation.[14,17] Competition ensues between adiabatic and nonadiabatic pathways once the threshold for $NH_2(\tilde{A})$ has been reached ($\upsilon_2' \geq 3$). $NH_3(\tilde{A})$ that dissociates via markedly nonplanar configurations, thereby avoiding the conical intersection region, does so on the surface that correlates to $NH_2(\tilde{A})$. Loomis et al. used time-resolved Fourier transform infrared emission spectroscopy to investigate 193 nm NH_3 photodissociation.[14] They found a bimodal $NH_2(\tilde{A})$ rotational distribution that they attributed to near-planar and bent geometries that dissociate. Angular momentum conservation dictates that (for $J = 0$ parent) the angular momentum of NH_2 is equal and opposite the orbital angular momentum of the fragment pair.[13] Dissociation from $NH_3(\tilde{A})$ is rapid; i.e., ∼20 fs. Thus, out-of-plane bending is manifested as *a*-axis rotation of the $NH_2(\tilde{A})$ product.[14]

AsH_2 Internal Excitations. Given that a 193 nm photon prepares $AsH_3(\tilde{A})$ with significant ν_2 (umbrella) vibrational excitation, and in light of the similarities between AsH_3 and PH_3 and between AsH_2 and PH_2, it is reasonable to expect the participating pathways and dissociation dynamics of AsH_3 to resemble those of PH_3. For example, consider the different θ_{H-M-H} equilibrium values that exist between parent and product species. The equilibrium values of θ_{H-P-H} for $PH_3(\tilde{A})$ and $PH_2(\tilde{X})$ are 114° and 91.4°, respectively.[18,38] This large difference of 22.6° can lead to significant bending excitation in the $PH_2(\tilde{X})$ product that accrues via the diabatic surface that correlates $PH_3(\tilde{A})$ to $PH_2(\tilde{X})$.

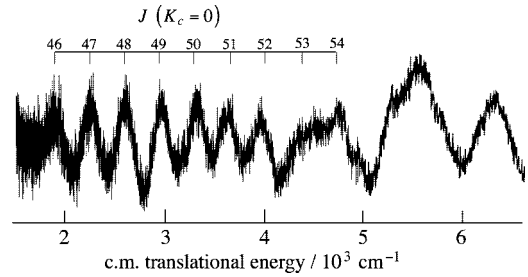

Figure 7. Low-energy features can be fit using high *J* values and various distributions of low K_c values.

Note that, in this regard, PH_3 differs (perhaps significantly) from NH_3. The equilibrium values of θ_{H-N-H} for $NH_3(\tilde{A})$ and $NH_2(\tilde{X})$ are 120° and 103.4°,[7] respectively: a change of 16.6°. This is 6° less than the 22.6° change that occurs with PH_3. Without a detailed calculation, however, it is not feasible to infer the degree of vibrational excitation present in the triatom product, given the θ_{H-M-H} equilibrium angles for a parent and its triatom product. Specifically, though the angular change in going from parent to products is large, the degree of vibrational adiabaticity along the reaction coordinate must be assessed.

Because of this vibrational adiabaticity, differences of 22.6° versus 16.6° might result in larger fractional differences in the degree of triatom bending excitation. For example, Lambert et al. observed PH_2 with substantial bending excitation and *a*-axis rotation following the ultraviolet photolysis of PH_3.[21] In contrast, it is known that NH_2 is formed with a relatively modest amount of bending excitation.[12−14,17]

The equilibrium bond angles for $AsH_3(\tilde{A})$ and $AsH_2(\tilde{X})$ are 112° (an estimate based on AsH_3^+ and $PH_3(\tilde{A})$) and 90.4°,[39] respectively. These values and their 21.6° difference are close to those of their PH_3 counterparts (114°, 91.4°, 22.6°, respectively). Thus, it is reasonable to expect AsH_2 to be formed with high internal excitation, specifically, *a*-axis rotation and bending excitation.

This is consistent with our data. The structure in the $P(E_{c.m.})$ distribution at low translational energies (Figure 6b) is consistent with $AsH_2(\tilde{X})$ having significant *a*-axis rotation. For example, to rationalize the peaks in Figure 6b, rotational energies for $AsH_2(\tilde{X})$, which is a near-oblate top ($\kappa = 0.8034$),[30] were calculated using the formula:

$$F(J, K_c) = \bar{B}J(J+1) + (C - \bar{B})K_c^2 \qquad (13)$$

where

$$\bar{B} = (A + B)/2 \qquad (14)$$

Values of rotational constants *A*, *B*, and *C* are 7.550, 7.162, and 3.615 cm^{-1}, respectively,[30] and $F(J, K_c)$ is the rotational energy.

Energy separations between calculated rotational levels matched the lower-energy spacings in Figure 6b. The structure below 5000 cm^{-1} is fit with *J* values in the range 46−54, as indicated in Figure 7. The large amount of $AsH_2(\tilde{X})$ internal energy, the complex energy disposal, and the scarcity of spectroscopic data make unique assignment impossible. Other sets of rotational levels also fit the data. However, the peaks cannot be fit using any reasonable choice of vibrational

frequencies. Moreover, the established propensity toward *a*-axis rotation is consistent with low K_c values. For example, including K_c values up to 10 does not alter the fit to the data indicated in Figure 7. The "bottom line" is that these estimates are consistent with $AsH_2(\tilde{X})$ being born with significant *a*-axis rotation.

Figure 6c highlights the structure present at the higher $E_{c.m.}$ values. Separations between peaks (though the data are of low S/N) are comparable to the bend of $AsH_2(\tilde{X})$.[30] Why does this structure occur at higher translational energy? Again, qualitative guidance is available from NH_3. $NH_3(\tilde{A})$ that retains near-C_{2v} symmetry during dissociation passes through the conical intersection region to form $NH_2(\tilde{X})$ in low rotational states.[12] Loomis et al. used an impulsive model to rationalize the efficient disposal of energy into NH_2 bending excitation for planar dissociation.[14] $AsH_3(\tilde{A})$ that remains near-planar during dissociation has a high probability of undergoing a nonadiabatic transition. The resulting $AsH_2(\tilde{X})$ will have bending excitation because of the change in equilibrium bond angle in going from $AsH_3(\tilde{A})$ to $AsH_2(\tilde{X})$ but less *a*-axis rotation than molecules that dissociate having considerable umbrella mode excitation.

Adiabatic and nonadiabatic transitions compete. $AsH_2(\tilde{A})$ arises from $AsH_3(\tilde{A})$ that dissociates mainly from geometries that avoid the conical intersection region. Therefore, $AsH_2(\tilde{A})$ is expected to have *a*-axis rotational excitation. Though the equilibrium angles of $AsH_3(\tilde{A})$ and $AsH_2(\tilde{A})$ (112° and 123°, respectively)[26,39] differ by a smaller amount than for $AsH_3(\tilde{A})$ and $AsH_2(\tilde{X})$ (112° and 90.4°, respectively),[26,39] it is not unreasonable to anticipate $AsH_2(\tilde{A})$ bending excitation.

$AsH_2(\tilde{A})$ is a near-prolate top ($\kappa = -0.8249$).[30] Rotational energies were estimated using $F(J, K_a) = \bar{B}J(J+1)+(A-\bar{B})K_a^2$, where $\bar{B} = (B-C)/2$, and *A*, *B*, and *C* values are 17.207, 4.920, and 3.740 cm^{-1}.[30] Peak separations in Figure 6b could not be fit using these calculated spacings.

Secondary Photolysis: $AsH_2 \rightarrow AsH + H$. Our considerations here are restricted to secondary photolysis processes that yield H atom fragments. Channels that yield H_2 are not considered. Figures 4−6 indicate that the photodissociation of AsH_3 yields AsH_2 with significant internal excitation and that this species is photolyzed. Energy conservation requires

$$h\nu_{193} + E_{AsH_2} - D_0(HAs - H) = E_{AsH} + E_{c.m.} \quad (17)$$

where E_{AsH_2} and E_{AsH} are the internal energies of AsH_2 and AsH, respectively. For those (infrequent) instances in which $E_{AsH_2} \approx D_0(HAs - H)$ and E_{AsH} is negligible, $E_{c.m.}$ is approximately equal to $h\nu_{193}$. In this case, the photon energy (51 780 cm^{-1}) appears as $E_{c.m.}$.

Indeed, the inset in Figure 6a indicates a fairly abrupt termination of $P(E_{c.m.})$ at 51 800 ± 500 cm^{-1}. This is also easy to see in the TOF spectrum in Figure 4. Namely, the arrival time for which $E_{c.m.} = h\nu_{193}$ is 12.4 μs, which coincides with the sharp onset of signal in the TOF spectrum. Thus, AsH_2 is formed with a distribution of internal energies that extends all the way up to $D_0(HAs - H)$.

Many channels are accessible when AsH_2 absorbs a 193 nm photon. Referring to Figure 2, photodissociation of $AsH_2(\tilde{X})$ from even its lowest rovibrational level can, on energetic grounds, access a number of product channels. Because AsH_2 contains significant internal excitation, the possibilities are legion.

Though $AsH(a\ ^1\Delta)$ and $AsH(b\ ^1\Sigma^+)$ are energetically accessible via secondary photolysis, emission from these species has not been observed following 193 nm excitation.[29] This can be due to the fact that singlet−triplet emission is weak or that these channels are not accessed. $AsH(A\ ^3\Pi)$ is energetically accessible when $AsH_2(\tilde{X})$ contains more than 1500 cm^{-1} of internal energy prior to its photoexcitation. Nonetheless, $AsH(A\ ^3\Pi)$ has not been detected in emission following 193 nm photolysis of AsH_3.

Photodissociation of $AsH_2(\tilde{X})$ that has $E_{AsH_2} \leq D_0(HAs - H)$ can, on energetic grounds, yield AsH(X) and AsH(A) with $E_{c.m.} \leq 51\,700\ cm^{-1}$ and $\leq 21\,700\ cm^{-1}$, respectively. The $E_{c.m.}$ distribution in Figure 6 is broad, peaking at ∼6000 cm^{-1}. Vibrational excitation in AsH is expected to be modest on the basis of changes of bond lengths: 1.483 Å in $AsH_2(\tilde{A})$,[39] 1.534 Å in AsH(X),[32] and 1.577 Å in AsH(A).[32] Though PESs are not available, possible pathways can be considered in light of symmetry and spin.[39] $AsH_2(\tilde{X}\ ^2B_1)$ and $AsH_2(\tilde{B}\ ^4B_1)$ correlate to $AsH(X\ ^3\Sigma^-) + H(^2S)$, whereas $AsH_2(\tilde{A}\ ^2A_1)$ does not correlate to $AsH(X\ ^3\Sigma^-)$. For PH_2, it has been noted that $\tilde{A}$ may predissociate via $^4B_1$ because of spin−orbit interaction.[40] However, $^4B_1$ is much higher in energy than $^2A_1$, so predissociation of $^2A_1$ via $^4B_1$ is considered unlikely in the present experiments.

V. Conclusions

(1) HRTOF spectroscopy has been used to examine the 193 nm photodissociation of AsH_3. Contributions from secondary AsH_2 photodissociation are also present. The degree of secondary photodissociation can be minimized, but not eliminated, by using low 193 nm fluences. The experimental method is sensitive only to product channels that give H atoms; that is, an elimination channel such as $AsH_2 \rightarrow As + H_2$ cannot be detected using the present arrangement. The main experimental result is a broad $P(E_{c.m.})$ distribution that contains a modest amount of superimposed structure.

(2) The dominant reaction pathway is $AsH_3 \rightarrow AsH_2(\tilde{X}) + H$. Nascent $AsH_2(\tilde{X})$ has considerable rovibrational excitation. The average value of E_{AsH_2} is ≈16 300 cm^{-1}, which is ≈ 64% of the available energy: $E_{avail} = h\nu - D_0(H_2As - H)$. The distribution of E_{AsH_2} values extends to values as large as $D_0(HAs - H)$. For those cases in which $E_{AsH_2} \approx D_0(HAs - H)$ and E_{AsH} is negligible, AsH_2 photodissociation yields $E_{c.m.} \approx h\nu_{193}$. This is manifested as a fairly abrupt termination of $P(E_{c.m.})$ at 51 800 ± 500 cm^{-1} (inset in Figure 6a), which matches $h\nu_{193} = 51\,780\ cm^{-1}$. This confirms that AsH_2 is formed with a distribution of internal energies that extends all the way to $D_0(HAs - H)$.

(3) It is known that $AsH_2(\tilde{A})$ is produced because its fluorescence has been detected,[29] though its yield could not be determined in the fluorescence measurements. In the present experiments, its yield is found to be modest. This follows from the fact that $E_{c.m.}$ must be ≤5600 cm^{-1} for the $AsH_2(\tilde{A})$ channel (Figure 2), and this energy range accounts for a modest fraction of the observed $P(E_{c.m.})$ distribution. Thus, most of the reactive flux passes from electronically excited AsH_3 to ground electronic state products, presumably via a nonadiabatic transition mechanism similar to those of PH_3 and NH_3.

(4) The 193 nm photolysis of AsH_3 has much in common with that of PH_3. On the basis of the PH_3 experimental data and known PH_3, PH_2, AsH_3, and AsH_2 geometrical properties, AsH_2 bending excitation is expected. For example, note the differences between equilibrium angles θ_{H-M-H}: 114° → 91.4° for $PH_3(\tilde{A}) \rightarrow PH_2(\tilde{X})$, and 112° → 90.4° for $AsH_3(\tilde{A}) \rightarrow AsH_2(\tilde{X})$. The separations between adjacent peaks in the structure present in the *high-energy* region of the $P(E_{c.m.})$ distribution (Figure 6c) are in qualitative accord with $AsH_2(\tilde{X})$ bending quanta.

(5) Separations between adjacent peaks in the *low-energy* region of the $P(E_{c.m.})$ distribution are in accord with $AsH_2(\tilde{X})$ rotational levels. This is consistent with a mechanism in which

parent umbrella motion evolves to *a*-axis rotation of the $AsH_2(\tilde{X})$ product, as occurs with the lighter group-V hydrides.

(6) An experimental study of the photodissociation of jet-cooled AsH_2 samples in which there is no contribution from AsH_3 background would resolve a number of issues. For example, this could be achieved by photodissociating AsH_3 in a high-pressure quartz expansion channel and then photodissociating expansion-cooled AsH_2 in spectral regions where AsH_3 does not absorb radiation.

(7) Theory is in good shape for NH_3, but the same is not true for AsH_3. Accurate electronic structure calculations will go a long way toward elucidating mechanisms and provide a detailed quantitative understanding of the photophysics and photochemistry of the full range of group-V hydrides. It is imperative that calculations for the heavier species are done at a high level of theory if experimental results are to be reconciled with confidence.

Acknowledgment. This research was supported by the U.S. Department of Energy, Office of Basic Energy Sciences. We received many valuable inputs from Aleksey Alekseyev and Jessica Quinn.

References and Notes

(1) Donnelly, V. M.; Karlicek, R. F. *J. Appl. Phys.* **1982**, *53*, 6399.
(2) Pütz, N.; Heinecke, H.; Veuhoff, E.; Arens, G.; Heyen, M.; Lüth, H.; Balk, P. *J. Cryst. Growth* **1984**, *68*, 194.
(3) Kukimoto, H.; Ban, Y.; Komatsu, H.; Takechi, M.; Ishizaki, M. *J. Cryst. Growth* **1986**, *77*, 223.
(4) Aoyagi, Y.; Kanazawa, M.; Doi, A.; Iwai, S.; Namba, S. *J. Appl. Phys.* **1986**, *60*, 3131.
(5) Balasubramanian, K. *Relativistic Effects in Chemistry, Parts A and B*; Wiley & Sons: New York, 1997.
(6) Pitzer, K. *Acc. Chem. Res.* **1979**, *12*, 271.
(7) McCarthy, M. I.; Rosmus, P.; Werner, H. J.; Botshwina, P.; Vaida, V. *J. Chem. Phys.* **1987**, *86*, 6693.
(8) Ranu, R.; Peyerimhoff, S. D.; Buenker, R. J. *J. Mol. Spectrosc.* **1977**, *68*, 253.
(9) Rosmus, P.; Botschwina, P.; Werner, H. J.; Vaida, V.; Engelking, P. C.; McCarthy, M. I. *J. Chem. Phys.* **1987**, *86*, 6677.
(10) Nangia, S.; Truhlar, D. G. *J. Chem. Phys.* **2006**, *124*, 124309.
(11) Vaida, V.; McCarthy, M. I.; Engelking, P. C.; Rosmus, P.; Werner, H. J.; Botschwina, P. *J. Chem. Phys.* **1987**, *86*, 6669.
(12) Biesner, J.; Schnieder, L.; Ahlers, G.; Xie, X.; Welge, K. H.; Ashfold, M. N. R.; Dixon, R. N. *J. Chem. Phys.* **1988**, *88*, 3607.
(13) Mordaunt, D.; Ashfold, M. N. R.; Dixon, R. N. *J. Chem. Phys.* **1996**, *104*, 6460.
(14) Loomis, R. A.; Reid, J. P.; Leone, S. *J. Chem. Phys.* **2000**, *112*, 658.
(15) Kassab, E.; Gleghorn, J. T.; Evleth, E. M. *J. Am. Chem. Soc.* **1983**, *105*, 1746.
(16) Hause, M. L.; Yoon, Y. H.; Crim, F. F. *J. Chem. Phys.* **2006**, *125*, 174309.
(17) Biesner, J.; Schnieder, L.; Ahlers, G.; Xie, X.; Welge, K. H.; Ashfold, M. N. R.; Dixon, R. N. *J. Chem. Phys.* **1989**, *91*, 2901.
(18) Müller, J.; Ågren, H. *J. Chem. Phys.* **1982**, *76*, 5060.
(19) Humphries, C. M.; Walsh, A. D.; Warsop, P. A. *Discuss. Faraday Soc.* **1963**, *35*, 148.
(20) Maripuu, R.; Reineck, I.; Ågren, H.; Nian-Zu, W.; Rong, J. M.; Veenhuizen, H.; Al-Shamma, S. H.; Karlsson, L.; Siegbahn, K. *Mol. Phys.* **1983**, *48*, 1255.
(21) Lambert, I. R.; Morley, G. P.; Mordaunt, D. H.; Ashfold, M. N. R.; Dixon, R. N. *Can. J. Chem.* **1994**, *72*, 977.
(22) Baugh, D.; Koplitz, B.; Xu, Z.; Wittig, C. *J. Chem. Phys.* **1988**, *88*, 879.
(23) Sam, C. L.; Yardley, J. T. *J. Chem. Phys.* **1978**, *69*, 4621.
(24) Berkowitz, J. *J. Chem. Phys.* **1988**, *89*, 7065.
(25) Potts, A. W.; Price, W. C. *Proc. R. Soc. London, Ser. A* **1972**, *326*, 181.
(26) Dai, D.; Balasubramanian, K. *J. Chem. Phys.* **1990**, *93*, 1837.
(27) Binning, R. C., Jr; Curtiss, L. A. *J. Chem. Phys.* **1990**, *92*, 1860.
(28) Koplitz, B.; Xu, Z.; Wittig, C. *Appl. Phys. Lett.* **1988**, *52*, 860.
(29) Ni, T.; Lu, Q.; Ma, X.; Yu, S.; Kong, F. *Chem. Phys. Lett.* **1986**, *126*, 417.
(30) He, S.-G.; Clouthier, D. J. *J. Chem. Phys.* **2007**, *126*, 154312.
(31) Balasubramanian, K; Nannegari, V. *J. Mol. Spectrosc.* **1989**, *138*, 482.
(32) Dixon, R. N.; Lamberton, H. M. *J. Mol. Spectrosc.* **1968**, *25*, 12.
(33) Aren, M.; Richter, W. *J. Chem. Phys.* **1990**, *93*, 7094.
(34) Buetel, M.; Setzer, K. D.; Shestakov, O.; Fink, E. H. *J. Mol. Spectrosc.* **1996**, *178*, 165.
(35) Moore, C. E. *Atomic Energy Levels*; National Bureau of Standards: Washington, DC, 1971.
(36) Zhang, J.; Riehn, C. W.; Dulligan, M.; Wittig, C. *J. Chem. Phys.* **1996**, *104*, 7027.
(37) Walsh, A. D. *J. Chem. Soc.* **1953**, 2296.
(38) Berthou, J. M.; Pascat, B.; Guenebaut, H.; Ramsay, D. A. *Can. J. Phys.* **1972**, *50*, 2265.
(39) Dixon, R. N.; Duxbury, G.; Lamberton, H. M. *Proc. R. Soc. London, Ser. A* **1968**, *305*, 271.
(40) Xuan, C. N.; Margani, A. *J. Chem. Phys.* **1994**, *100*, 7000.

JP8094769